IOPscience iopscience.iop.org

Home Search Collections Journals About Contact us My IOPscience

Role of surface-active elements during keyhole-mode laser welding

This article has been downloaded from IOPscience. Please scroll down to see the full text article.

2011 J. Phys. D: Appl. Phys. 44 485203

(http://iopscience.iop.org/0022-3727/44/48/485203)

View the table of contents for this issue, or go to the journal homepage for more

Download details:
IP Address: 71.58.210.5
The article was downloaded on 20/11/2011 at 17:15

Please note that terms and conditions apply.

IOP PUBLISHING JOURNAL OF PHYSICS D: APPLIED PHYSICS

J. Phys. D: Appl. Phys. **44** (2011) 485203 (10pp) doi:10.1088/0022-3727/44/48/485203

Role of surface-active elements during keyhole-mode laser welding

B Ribic[1], S Tsukamoto[2], R Rai[1] and T DebRoy[1]

[1] Department of Materials Science and Engineering The Pennsylvania State University, University Park, PA 16802, USA

[2] National Institute for Materials Science, Structural Engineering Group, 1-2-1, Sengen, Tsukuba 304-0047, Japan

E-mail: debroy@psu.edu

Received 1 June 2011, in final form 15 October 2011
Published 18 November 2011
Online at stacks.iop.org/JPhysD/44/485203

Abstract

During high power density laser welding of mild steel, the keyhole depth, liquid metal flow, weld geometry and weld integrity are affected by base-metal sulfur content and oxygen (O_2) present in the atmosphere or shielding gas. The role of these surface-active elements during keyhole-mode laser welding of steels is not well understood. In order to better understand their effects, welding of mild steel specimens containing various concentrations of oxygen and sulfur are examined. In addition, a numerical model is used to evaluate the influence of the surface-active elements on heat transfer and fluid flow in keyhole-mode laser welding. Increase in base-metal sulfur concentration or O_2 content of shielding gas results in decreased weld widths. Sulfur results in a negligible increase in penetration depth whereas the presence of O_2 in shielding gas significantly affects the weld penetration. It has earlier been proposed that oxygen, if present in the shielding gas, can get introduced into the weld pool resulting in formation of carbon monoxide (CO) at the keyhole surface and additional pressure from CO can result in increased penetration. Numerical modelling has been used in this work to understand the effects of formation of CO on the keyhole and weld geometries.

(Some figures may appear in colour only in the online journal)

1. Introduction

The interaction of a high power density laser beam with the workpiece surface can result in rapid vaporization of the workpiece material and the formation of a narrow, deep, vapour filled cavity called a keyhole [1, 2]. The presence of surface-active elements (sulfur, oxygen) in steels and O_2 in the surrounding environment can significantly affect the geometry of fusion welds [3–8]. While the role of surface-active elements during arc welding [9–14] and low power density (less than 10^5 W cm^{-2}) laser welding [7, 15–18] has been extensively studied in the past, their influence during high power density keyhole-mode laser and laser–arc hybrid welding is not well understood. Sulfur is commonly present in steels whereas oxygen is often introduced into the workpiece from the atmosphere or shielding gas [6]. The presence of surface-active elements in the workpiece can influence weld pool fluid flow, convective heat transport and weld bead geometry by changing the surface-tension gradient [7, 19–25]. In the case of high power density laser welding and laser–arc hybrid welding, it has been reported that increasing the O_2 concentration in the environment reduces weld width and increases weld penetration depth [6]. The effects of O_2 present in the environment on weld geometry have been attributed to its effect on surface-tension driven flow [6], enhanced absorption of laser energy [6] and the pressure exerted by formation of gaseous CO [8]. No definite mechanism for the behaviour of oxygen in keyhole-mode welding has been established.

Naito *et al* [6] observed that increasing O_2 content in the environment of the workpiece resulted in deeper penetration and narrower weld width for keyhole-mode laser and laser–arc hybrid welds. The post-weld oxygen concentration in the weld metal was found to be greater for welds made under environments with higher O_2 concentrations [6]. X-ray measurements showed that the direction of fluid flow at the top surface was reversed when O_2 was present in the atmosphere compared with when welding was done under pure argon atmosphere [6]. This effect of dissolved oxygen

 © 2011 IOP Publishing Ltd Printed in the UK & the USA

on Marangoni convection near the top surface was related to a lack of 'nail head' shape in welds which were made in O_2 containing environments [6]. However, since the presence of dissolved oxygen did not alter the direction of fluid flow along the keyhole walls, except at small distances from the top surface, the influence of surface-active element effect on penetration depth was not directly evident. Aidun and Martin [4] reported that the penetration for a keyhole-mode laser weld made on 316 stainless steel with 0.006 wt% sulfur was greater than that for a weld made on the same material but containing 0.001 wt% sulfur. However, two welds made on 304 stainless steel containing 0.003 wt% and 0.008 wt% sulfur showed similar penetration depths [4]. Gas-tungsten-arc (GTA) weld penetration was affected more strongly by increase in O_2 content in shielding gas (100% Ar to 99Ar–$1O_2$) than by increasing sulfur concentration. Greater weld penetration during GTA welding was attributed to a hotter arc for 99Ar–$1O_2$ shielding gas compared with that for pure Ar [4].

Welds made under the same welding parameters can have somewhat different penetration depths and weld widths, often in different transverse sections of the same weld. This is particularly true of keyhole-mode welds which can have fluctuating keyholes. Therefore, variation in weld dimensions with change in any process variable (for example, sulfur or oxygen content) should be compared with the scatter in weld dimensions for the same welding conditions. Such statistical studies of the effect of oxygen and sulfur on keyhole-mode welds have not been reported in the open peer-reviewed literature.

Since convection is significant during high power laser welding and laser/GTA hybrid welding, the presence of surface-active elements can impact the weld bead geometry by influencing the fluid flow within the liquid weld pool [25–27]. The various driving forces for the liquid metal fluid flow are buoyancy, electromagnetic, surface tension and shear or frictional driven forces [7, 22, 25, 28, 29]. However, they are not equally important for the fluid flow in the molten weld pool during laser and hybrid welding. The primary driving force affecting fluid flow during laser welding is the Marangoni stress, which arises from the spatial gradient of surface tension driven by the temperature and compositional gradients existing in the weld pool [24–26, 28]. The Marangoni stress (τ) is defined by [22]

$$\tau = \frac{\mathrm{d}\gamma}{\mathrm{d}T}\frac{\mathrm{d}T}{\mathrm{d}y}, \tag{1}$$

where $\mathrm{d}\gamma/\mathrm{d}T$ is the temperature coefficient of surface tension and $\mathrm{d}T/\mathrm{d}y$ is the spatial temperature gradient on the weld pool surface. The presence of surface-active elements such as sulfur and oxygen in the steel weld pools has an impact on the magnitude and direction of convection [30]. If surface-active elements are not present in the weld pool, the $\mathrm{d}\gamma/\mathrm{d}T$ term is negative, and liquid metal flows outwards from the heat source along the surface of the weld pool [7, 30]. Outward flow from the heat source causes the weld pool to become wider [7]. If high concentrations of surface-active elements are present in the weld pool, the $\mathrm{d}\gamma/\mathrm{d}T$ term may become positive depending on the local temperature and the concentration of the surface-active element, thereby reversing the local direction of liquid metal flow [7, 30].

Zhao *et al* [8] showed that the penetration depth in keyhole-mode laser welding coincides with the keyhole depth. They argued that the changes in fluid flow induced by the presence of dissolved O_2 do not affect the keyhole depth. They proposed, instead, that formation of gaseous CO in the keyhole could influence the keyhole shape by exerting a pressure on the keyhole walls [8]. However, a quantitative understanding of the influence of CO formation on keyhole geometry remains to be developed.

Experimentally, it is difficult to determine the influence of CO pressure on the laser generated keyhole. High temperatures, the presence of metal vapours and plasma, and the small size of the keyhole, all make experimental measurements very difficult. Numerical modelling has previously offered a means of successfully evaluating the roles of heat transfer and fluid flow during high power density laser welding and laser–arc hybrid welding [24–26]. Several models have been proposed which included the influence of pressures acting inside the keyhole [17, 31–34]. However, these models did not consider the influence of surface-active elements [17, 31–34]. Fuhrich *et al* [35] considered the fluid flow in keyhole-mode laser welding of steel using a fixed keyhole geometry and a constant $\mathrm{d}\gamma/\mathrm{d}T$ for two cases: (1) a positive value of $\mathrm{d}\gamma/\mathrm{d}T$ and (2) a negative value of $\mathrm{d}\gamma/\mathrm{d}T$. They suggested that the presence of surface-active elements causes downward fluid flow at keyhole walls by making $\mathrm{d}\gamma/\mathrm{d}T$ positive and leads to deeper penetration welds [35]. However, it is known that the effect of surface-active elements on $\mathrm{d}\gamma/\mathrm{d}T$ of liquid steel is limited to temperatures much below the boiling point [30]. Furthermore, temperature variation along the keyhole walls is very small in laser beam welding and the temperature is often assumed to be constant [23–25]. Therefore, the magnitude of the surface-tension gradient along the keyhole walls is small in keyhole-mode laser beam welding [23–25]. Finally, experimental results presented in this work show that sulfur does not influence keyhole penetration. As a result, it seems unlikely that the effect of surface-active elements on fluid flow is primarily responsible for the increase in penetration depth when O_2 is added to the shielding gas.

Here we critically examine the roles of sulfur concentration in the steel and oxygen concentration in the shielding gas on the keyhole-mode Yb doped fibre laser welding of mild steel. The results are statistically analysed to rigorously evaluate the effects of O_2 in the shielding gas and sulfur in the base metal. For the welding conditions considered in this study, the presence of O_2 in the shielding gas affected both weld penetration and weld width, whereas sulfur influenced only weld width. A numerical model of heat transfer and fluid flow is used to understand the effect of CO formation on the weld geometry as the O_2 content in shielding gas increases. The model incorporates the influence of surface-active elements such as oxygen and sulfur in the calculation of temperature and fluid velocity profiles.

2. Mathematical model

The governing equations and the boundary conditions for the solution of the equations of conservation of mass, momentum

and energy are available in the literature [23–25, 29, 30] and are not repeated here. Instead, only the mathematical description of the salient features of the specific physical processes that are unique for this paper are presented here.

2.1. Keyhole calculation

The keyhole geometry calculation is done in two stages. In the first stage, an initial keyhole shape is determined through an iterative process before the heat transfer and fluid flow calculations commence. In the second stage, this initial keyhole shape is modified during the three-dimensional heat transfer and fluid flow calculations.

First stage. The iterative calculation of the initial keyhole geometry is based on a point-by-point energy and pressure balance at the keyhole walls [2, 23–26, 36, 37]. In the energy balance at keyhole walls, heat transport is assumed to be mainly along the horizontal direction due to the nearly vertical shape of keyhole and small temperature gradient along the depth. The heat balance equation is given as

$$\tan\theta = \frac{I_c}{I_a - I_v/\sin\theta}, \tag{2}$$

where θ is the local inclination of the keyhole wall with the vertical, I_c is the heat flux conducted into the workpiece, I_a is the heat flux absorbed and I_v is the heat flux used in vaporization. For the estimation of I_c, the temperature field in the workpiece is approximated by Rosenthal's line source model [2, 24, 25, 36].

In the first iteration of the solution for the initial keyhole geometry based on equation (2), keyhole wall temperature is taken as the normal boiling point of the alloy at 1 atm [2, 24], energy absorption is defined by the Fresnel absorption coefficient [2, 23, 24, 26] and $\sin\theta$ is taken as one. After the calculation of keyhole geometry in the first iteration, the keyhole wall temperature at any depth is taken as the temperature at which the local pressure balance at keyhole walls is satisfied [37–39]:

$$P_r + P_v + P_{CO} = P_\gamma + P_0 + \rho_l g h, \tag{3}$$

where P_r is the recoil pressure, [40] P_v is the pressure of metal vapours, P_{CO} is the equilibrium pressure due to CO formation in the keyhole, P_γ is the surface-tension pressure, [39] P_0 is the ambient pressure, ρ_l is the liquid density, g is the gravitational acceleration and h is the local keyhole depth. After the first iteration, the effect of multiple reflections of the laser beam inside the keyhole is also considered using an effective absorption coefficient based on the keyhole geometry calculated in the previous iteration [2, 23, 24, 26]. The keyhole geometry is recalculated based on equation (2) using the new keyhole wall temperatures, effective absorption coefficients and value of $\sin\theta$ estimated from the keyhole geometry in previous iterations. The iterative process of determining the initial keyhole geometry ceases when the keyhole temperature profile and depth converge. Detailed discussions of the keyhole calculation [2, 23–26, 41] are available in the literature.

The dissolved oxygen content of the weld metal affects the partial pressure of carbon monoxide (CO) in the keyhole. CO may form at the keyhole walls through the combination of dissolved carbon and oxygen: [C] + [O] = CO(g). The standard energy change for this reaction (ΔG^o) in J mol^{-1} is equal to ($-22\,390.0 - 39.7 \times T$), where temperature ($T$) is in Kelvin [42–44]. The standard free energy change was used to determine the reaction equilibrium constant, K_{eq} from the relation $\Delta G^o = -RT \ln K_{eq}$ in order to estimate the equilibrium partial pressure of CO. The equilibrium constant for the formation of CO is defined by [42]

$$K_{eq} = \frac{P_{CO}}{a_C a_O}, \tag{4}$$

where a_C and a_O are the activities of dissolved carbon and oxygen in the steel. The activity of the dissolved species is defined by [42]

$$a_i = \gamma_i^o(\%i), \tag{5}$$

where $\%i$ is the weight per cent of element i in the alloy and γ_i^o is the activity coefficient of element i, which is defined by [42]

$$\log \gamma_i^o = e_i^i(\%i) + \sum e_i^j(\%j), \tag{6}$$

where e_i^i is the first order interaction coefficient for the solute and e_i^j is the first order interaction coefficient which accounts for the effect of the alloying element j on the activity coefficient of the solute i. The oxygen concentration in the weld metal was measured after welding at two depths along the centre of weld cross-section. The carbon and sulfur concentrations were taken from the nominal material composition before welding. The activity coefficients were determined using the first order interaction coefficients from Sigworth and Elliott [44].

The partial pressure of CO near the keyhole walls depends not only on the reaction thermodynamics but also the kinetic factors such as diffusion of solute atoms through the interfacial boundary layers. The equilibrium partial pressure of a gas calculated based on the reaction constants and bulk solute concentrations can be considered the maximum possible value of the actual gas pressure at the keyhole walls. The pressure of CO at the keyhole walls was taken as a constant factor times the equilibrium pressure calculated using bulk concentrations of dissolved oxygen and carbon. The choice of this factor (= 0.8) is discussed in section 5.3.

Second stage. After the calculation of initial keyhole geometry, the heat transfer and fluid flow calculations commence. A check for the consistency between laser power absorbed and heat conducted from the keyhole walls into the workpiece is performed as

$$\sum F_i A_i = H_a - H_v, \tag{7}$$

where F_i is the heat flux at location i on the keyhole wall, A_i is the local area transverse to the flux direction at location i, H_a is the heat absorbed at the keyhole wall and H_v is the total evaporative heat loss. If the calculations deviate significantly from equation (7), the keyhole geometry is modified. This is accomplished by adjusting the power per unit depth and recalculating the keyhole geometry until equation (7)

is satisfied. The procedure for calculating keyhole geometry has been discussed by Zhao *et al* [2]. As the keyhole size is modified, the keyhole wall temperatures are recalculated based on the solution of pressure balance equation (3) for the modified keyhole geometry.

2.2. Heat and fluid flow in weld pool

The heat and fluid flow model has been extensively documented previously [2, 23–25] and will only be briefly described here. The numerical model solves the equations of conservation of mass, momentum and energy in three-dimensions for the solid, liquid and solid–liquid regions. The model considers buoyancy, surface-tension driven flow [18, 22, 30, 45], thermal expansion, mushy zone morphology, enhancement of viscosity and thermal conductivity due to weld pool turbulence and heat transport through conduction, convection and radiation [2, 23–25]. The heat source is approximated as a Gaussian distribution [1, 24, 25]. The numerical model uses measured weld metal sulfur and oxygen concentrations to determine the surface-tension gradient and its influence on the weld metal fluid flow. The temperature coefficient of surface tension was calculated using a formulation [30] that is widely used in the literature.

3. Experimental procedure

Yb doped fibre laser welding was performed on 20 mm thick mild steel at sharp focus. The laser power was 7 kW and the beam radius at the focal point was 200 μm. The laser beam characteristic wavelength was between 1070 and 1080 nm. The welding speed for all cases was 16.7 mm s^{-1}. The alloy sulfur content was specifically varied for the Yb doped fibre laser welds to analyse the influence of sulfur on the heat transfer and fluid flow for a constant percentage of O_2 (0%) in the shielding gas. The various base-metal sulfur concentrations were 0.006, 0.015, 0.056, 0.077, 0.101 and 0.150 wt%. The chemical composition of the mild steel samples [25, 26, 46] is provided in table 1. Various shielding gas compositions were also used for a constant concentration of sulfur in the base metal of 0.006 wt%. Three gases were mixed in a gas mixer where the flow rate of each gas was measured to 0.1 L min^{-1} accuracy. The gas composition was controlled by adjusting the flow rate of each gas. The shielding gas compositions were 61% He + Ar, 58% He + Ar + 5% O_2, 55% He + Ar + 10% O_2 and 52% He + Ar + 15% O_2 and the corresponding concentrations of oxygen in the weld metal were measured after welding. In addition, oxygen concentrations in the upper and lower halves of the weld bead were measured along the weld centreline. The measured oxygen concentrations in the lower half were [47] 0.0038 wt% (0% O_2), 0.0078 wt% (5% O_2), 0.0135 wt% (10% O_2) and 0.0257 wt% (15% O_2). The measured oxygen concentrations in the upper half were 0.0044 wt% (0% O_2), 0.0101 wt% (5% O_2), 0.0182 wt% (10% O_2) and 0.0358 wt% (15% O_2). The shielding gas flow rate was 0.42 L s^{-1}. The material properties [25, 26, 46] used for the welding calculations are presented in table 2.

Table 1. Chemical composition of mild steel samples.

	Element						
	C	Mn	Si	P	S	O	N
wt%	0.16	1.46	0.35	0.016	0.006, 0.015, 0.056 0.077, 0.101, 0.15	0.001	0.0025

Table 2. Material properties for the mild steel used in the welding calculations.

Material	Mild steel
Density of the liquid (kg m^{-3}) [25]	7000
Density at the boiling point (kg m^{-3}) [25]	5800
Solidus temperature (K) [25]	1745
Liquidus temperature (K) [25]	1785
Enthalpy of solid at melting point (J kg^{-1}) [25]	1.20E + 06
Enthalpy of liquid at melting point (J kg^{-1}) [25]	1.26E + 06
Specific heat of solid (J kg^{-1} K^{-1}) [25]	711
Specific heat of liquid (J kg^{-1} K^{-1}) [25]	795
Thermal conductivity (W m^{-1} K^{-1}) [26]	21
Coefficient of thermal expansion (1 K^{-1}) [46]	$1.30E-05$
$d\gamma/dT$ of pure material (N m^{-1} K^{-1}) [25]	−0.000 49
Surface excess at saturation (mole m^{-2}) [25]	$1.30E-05$
Enthalpy of segregation (J mol^{-1}) [25]	$-1.66E+05$
Entropy factor [25]	0.003 18

4. Data analysis

A single factor analysis of variance (ANOVA) was used to statistically evaluate if weld bead depth and width differed significantly with increasing concentrations of O_2 in the shielding gas and of sulfur in the base metal with 95% confidence. Twenty weld pool depths and twenty widths were measured to examine the effect of oxygen. Four cross sections were evaluated for each of the two highest levels of oxygen, and six cross sections each were examined for the other two levels. Thirty weld pool depths and thirty widths were examined to evaluate the effect of sulfur. Six cross sections each were evaluated for the lowest and two highest sulfur concentrations and four cross sections each for the other three levels. The ANOVA assesses whether the expected values of a variable within several groups of observations differ from each other. For example, if the expected values of the weld depth differ statistically for various groups of oxygen concentrations, the weld depth is thought to vary with oxygen concentration and the calculated F statistic is greater than a critical value. The critical value is dependent upon the number of observations and concentration levels considered. The F statistic is a ratio of the variability between groups and within group variability. When the F statistic is large and the within group variability is small, there is a correlation between the increasing surface-active element concentration and the measured weld dimension. Correspondingly, the P value will be less than 5%. The P value assesses the likelihood that a given surface-active element concentration has no influence on the considered weld dimension [48]. The details of the calculation of F statistic are provided in the appendix.

Table 3. ANOVA results for the influence of sulfur and weld metal oxygen concentrations on laser weld bead depth and width.

Parameter/Attribute	F value	P value	F critical
Sulfur			
Depth	0.63	0.68	2.62
Width	40.45	6.30E − 11	2.62
Oxygen			
Depth	42.56	7.50E − 08	3.24
Width	99.32	1.48E − 10	3.24

5. Results and discussion

5.1. Statistical analysis of the effect of base-metal sulfur and oxygen concentrations

Table 3 shows the ANOVA results for the influence of weld metal sulfur and oxygen concentrations on measured laser weld bead width and depth. The P value is the probability of obtaining an F value equal to that calculated from experimental data, assuming that the null hypothesis is true. Conversely, for a given F value, a high P value implies greater probability that the null hypothesis is true. The null hypothesis may be rejected if the P value is lower than 0.05 (for a 95% confidence interval). Table 3 shows that the null hypothesis—i.e. the sulfur content does not influence the weld dimension—can be rejected for width, but not for depth. In other words, the effect of base-metal sulfur content is statistically significant for weld width but not for weld depth. The low P values show that the variation of measured depth as well as measured width due to change in O_2 content in shielding gas is statistically significant.

5.2. Effect of sulfur: experimental and computational study

Figure 1 shows variation of the experimental and calculated laser weld (a) depths and (b) widths as a function of the sulfur concentration in the base metal. Standard error bars are shown for the mean measured depths and widths. Figure 1 shows that increasing the concentration of sulfur in the base metal, over the range considered here, significantly influenced the measured weld bead width but did not appreciably affect the measured weld pool depth. The calculated penetration depth agrees reasonably well with the measured values as shown in figure 1(a). The variation of calculated weld width with increasing sulfur content is qualitatively similar to the experiments, although there is some difference in the calculated and measured values at high sulfur concentrations. The higher experimental weld widths may be due to lower effective sulfur concentrations on the surface as a result of evaporation.

The decrease in laser weld width with increasing sulfur concentration, as shown in figure 1(b), is due to changes in heat and fluid transport in the molten weld pool. The average errors between the experimental and calculated weld dimensions were 1.3% for weld depth and 17.7% for weld width. At low sulfur concentrations (<0.002 wt%), $\mathrm{d}\gamma/\mathrm{d}T$ at the top surface is negative. This drives the fluid near the top surface outward forming convection currents that result in enhanced heat transport near the top surface and widening of weld pool

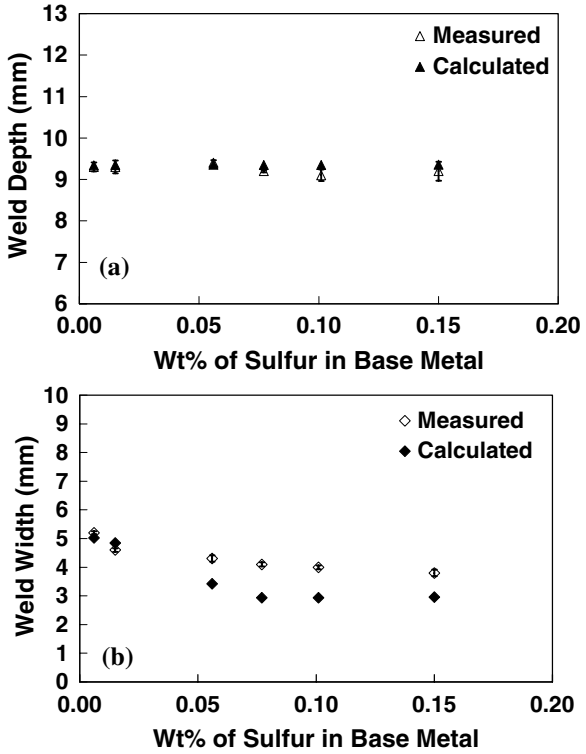

Figure 1. Plots comparing the experimental and calculated laser weld (a) depths and (b) widths as a function of the sulfur concentration in the base metal. Standard error bars are shown for the measured weld dimensions.

near the top surface. The effect on increasing sulfur content on the fluid flow and weld width is discussed below with the help of figure 2.

Figure 2 shows calculated three-dimensional temperature and fluid flow profiles for the laser welded mild steel containing (a) 0.015 wt%, (b) 0.056 wt% and (c) 0.101 wt% sulfur. When the sulfur concentration is above 0.002 wt%, $\mathrm{d}\gamma/\mathrm{d}T$ depends on the local temperature. At temperatures close to the solidus, $\mathrm{d}\gamma/\mathrm{d}T$ is positive and fluid flow is inwards. At higher temperatures close to the keyhole, $\mathrm{d}\gamma/\mathrm{d}T$ is negative and fluid flow is outwards. The two flows meet somewhere between the solid–liquid boundary and the keyhole walls resulting in two circulating currents. The location where the two flows meet depends on the sulfur concentrations and the local temperatures; as sulfur concentration increases, this location moves closer to the keyhole.

A laser weld with medium sulfur concentration (0.015 wt%) is shown in figure 2(a). The fluid moving away from the keyhole (and carrying heat) is limited to a small distance from the keyhole walls due to the opposing flow from the weld pool boundary. At sulfur concentrations greater than 0.03 wt% (figure 2(b)), when the fluid flow is predominantly inwards, the circulation current due to outward flow on the top surface is much smaller and limited to a very small region near the top surface. As the sulfur content approaches concentrations of 0.101 wt% (figure 2(c)) and 0.150 wt%, the size of the region where fluid flow is towards the solid/liquid boundary reduces in size. However, weak radially outward flow is present near the keyhole walls even at these very high

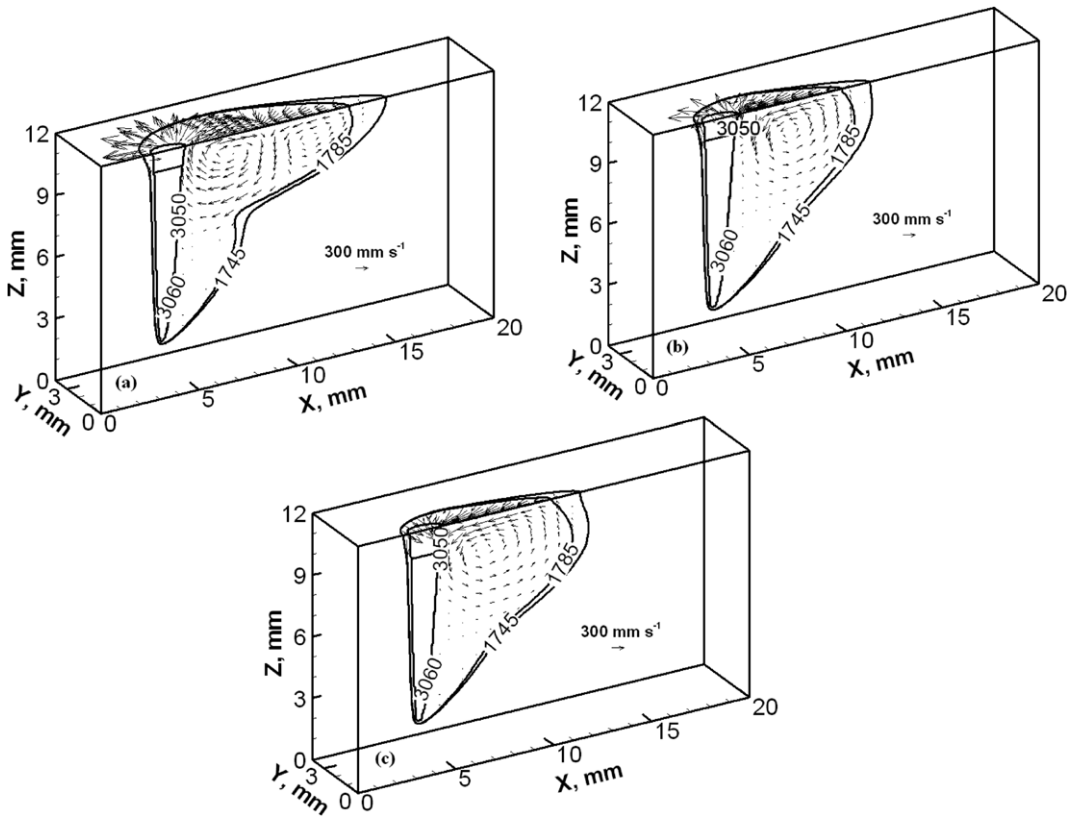

Figure 2. Calculated three-dimensional temperature and fluid flow profiles during 7 kW laser welding of mild steel containing (*a*) 0.015 wt%, (*b*) 0.056 wt% and (*c*) 0.101 wt% sulfur.

sulfur concentrations. In other words, fluid flow at top surface becomes increasing inwards with greater sulfur content leading to less heat transport in radially outward direction and narrower welds.

Figure 3 shows comparison of the calculated and experimental weld cross sections for the laser welded sample for 0% O_2 in shielding gas (i.e. approximately 0.0038 wt% oxygen in base metal) and (*a*) 0.006 wt%, (*b*) 0.015 wt%, (*c*) 0.056 wt%, (*d*) 0.077 wt%, (*e*) 0.101 wt% and (*f*) 0.150 wt% sulfur. The calculated weld geometries agree reasonably well with the experimental results. With increasing sulfur concentration in the weld pool, the weld width decreases due to the top surface fluid flow direction becoming more radially inward from the solid/liquid boundary.

Of the various pressure terms in equation (3), the most significant pressures in the keyhole are the vapour pressure, surface-tension pressure and pressure of CO. Table 4 shows the calculated pressures used to determine the keyhole wall temperatures for different sulfur concentrations. $\mathrm{d}\gamma/\mathrm{d}T$ at keyhole walls is not affected by the sulfur content of the base metal due to the high wall temperatures. The effect of sulfur concentration on the activities of dissolved oxygen and carbon, and consequently, on the CO pressure is negligible. Due to the very small variation in the various pressure terms as shown in table 4, the keyhole wall temperatures varied negligibly, and a constant penetration of 9.3 mm was obtained throughout the range of sulfur concentrations considered. It has been shown that the keyhole and weld penetration depth during laser and laser–arc hybrid welding are similar [1, 24]. Since increasing the concentration of sulfur in the base metal results in a negligible change in keyhole depth, the penetration depth does not change significantly. It should be noted that the conclusion regarding the effect of sulfur on penetration depth applies only to the range of process conditions and workpiece material considered in this work. To the best of our knowledge, this is the first statistical study of the influence of sulfur on the penetration depth of keyhole-mode laser welds.

5.3. Effect of oxygen: experimental and computational study

Table 5 shows the various computed pressures at the keyhole walls when 0%, 5%, 10% and 15% O_2 is added to the shielding gas during 7 kW laser welding of mild steel. The significant terms in pressure balance are due to metal vapours and CO. As the oxygen concentration increases, the CO pressure increases significantly. As a result, the pressure balance at keyhole walls can be attained with lower keyhole wall temperatures. The lower wall temperatures permit increased keyhole penetration and somewhat narrow weld widths [41, 49]. In this work, CO pressure at keyhole walls for each case was taken as a fixed fraction of the equilibrium value calculated using bulk concentrations of dissolved oxygen and carbon. A factor of 0.8 was chosen for good agreement between experimental and calculated weld widths as oxygen concentration was varied (figure 4(*b*)).

The plots of the experimental and calculated laser weld depths and widths as functions of shielding gas O_2 percentage are shown in figure 4. Standard error bars have been added

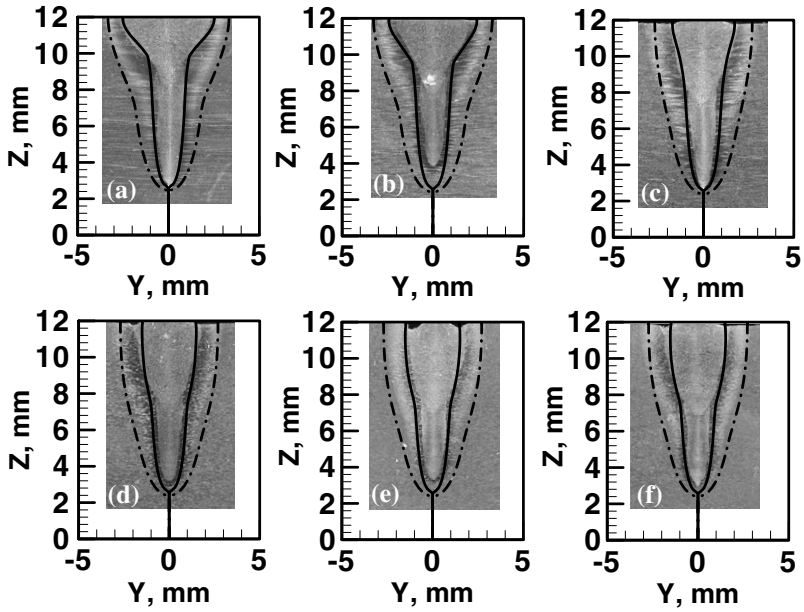

Figure 3. Comparison of calculated and measured 7 kW laser weld cross sections when the base metal contained (*a*) 0.006 wt%, (*b*) 0.015 wt%, (*c*) 0.056 wt%, (*d*) 0.077 wt%, (*e*) 0.101 wt% and (*f*) 0.150 wt% sulfur. The dotted line in the cross sections is the 1000 K isotherm and the solid line outlining the fusion zones is the 1745 K solidus isotherm.

Table 4. Calculated keyhole dimensions, keyhole wall temperature, and magnitudes of partial pressures acting at keyhole surface 4.5 mm below the top surface of the weld pool for various concentrations of sulfur in the base metal during 7 kW laser welding of mild steel.

Concentration of sulfur in base metal (wt%)	0.015	0.056	0.077	0.101	0.15
Total keyhole depth (mm)	9.30	9.30	9.30	9.30	9.30
Keyhole radius[a] (mm)	0.54	0.57	0.57	0.54	0.54
Keyhole wall temperature (K)	3052	3052	3052	3053	3053
Metal vapour pressure (atm)	9.24E − 01	9.23E − 01	9.24E − 01	9.26E − 01	9.27E − 01
Surface tension (N m^{-1})	1.41	1.41	1.41	1.41	1.41
Surface-tension pressure (atm)	2.57E − 02	2.44E − 02	2.44E − 02	2.57E − 02	2.57E − 02
Hydrostatic pressure (atm)	3.03E − 03	3.03E − 03	3.03E − 03	3.03E − 03	3.03E − 03
Recoil pressure (atm)	2.08E − 03	2.08E − 03	2.08E − 03	2.10E − 03	2.10E − 03
P_{CO} (atm)	0.103	0.102	0.101	0.101	0.100

[a] Keyhole radius reported here is half of the distance between the front and rear keyhole walls along the weld symmetry line 4.5 mm below the top surface.

for the experimental results. Figure 4 clearly shows that with increasing O_2 percentage in the shielding gas, the experimental weld widths decrease whereas the experimental weld depths increase. The decrease in weld width (figure 4(*b*)) with increasing oxygen content can be attributed to the effect of oxygen on Marangoni convection. Measured penetration depth was about 16% higher for Ar–15% O_2 shielding gas compared with the penetration depth with Ar–0% O_2 shielding gas. The calculated and experimental weld widths agree very well. However, present calculations somewhat under-predict the effects of increase in O_2 content of the shielding gas on the penetration depth, especially for 10% and 15% O_2 cases.

As discussed before, experimental weld penetration was not influenced by base-metal sulfur content. It should be noted that the sulfur concentrations were higher, and had larger variation, than oxygen concentrations in this study. Therefore the increase in the weld penetration due to O_2 content in shielding gas is not primarily due to the influence of surface-active oxygen on the fluid flow. It also seems that the effect of CO generation, as modelled in this study, can qualitatively explain the increase in penetration depth. The reasons for the lack of excellent agreement between the computed and the experimentally determined depth values (figure 4(*a*)) are not known.

Calculated and experimentally obtained weld cross sections when the shielding gas contained (*a*) 0%, (*b*) 5%, (*c*) 10%, (*d*) 15% O_2 are shown in figure 5. The computed weld geometries in figure 5 are in fair agreement with the experimental results.

Temperature and fluid velocity profiles calculated for 7 kW laser welding of mild steel for (*a*) 0% and (*b*) 10% O_2 in the shielding gas are shown in figure 6. The presence of oxygen and sulfur (0.006 wt% sulfur) causes radially inward flow towards the keyhole at the weld pool surface close to the weld pool solid/liquid boundary. Near the keyhole, the fluid flow is radially outward due to the relatively high liquid metal temperatures compared with the solid/liquid boundary. As the oxygen concentration increases in the liquid weld metal, the radially outward fluid flow decreases in magnitude and the radially inward flow increases. The increase in radially

Table 5. Calculated keyhole dimensions, local keyhole wall temperature, and magnitudes of partial pressures acting at keyhole surface 4.5 mm below the top surface of the weld pool when O_2 content of shielding gas is varied during 7 kW laser welding of mild steel.

% O_2 in shielding gas	0	5	10	15
Concentration of oxygen in weld metal (wt%)	0.0038	0.0078	0.0135	0.0257
Keyhole depth (mm)	9.30	9.39	9.59	10.1
Keyhole radius[a] (mm)	0.51	0.54	0.60	0.75
Keyhole wall temperature (K)	3052	3023	2972	2782
Metal vapour pressure (atm)	9.25E − 01	8.15E − 01	6.52E − 01	2.69E − 01
Surface tension (N m^{-1})	1.41	1.42	1.44	1.52
Surface-tension pressure (atm)	2.73E − 02	2.60E − 02	2.37E − 02	2.01E − 02
Hydrostatic pressure (atm)	3.03E − 03	3.03E − 03	3.03E − 03	3.03E − 03
Recoil Pressure (atm)	2.08E − 03	1.64E − 03	1.07E − 03	1.94E − 04
P_{CO} (atm)	0.10	0.21	0.37	0.75

[a] Keyhole radius reported here is half of the distance between the front and rear keyhole walls along the weld symmetry line 4.5 mm below the top surface.

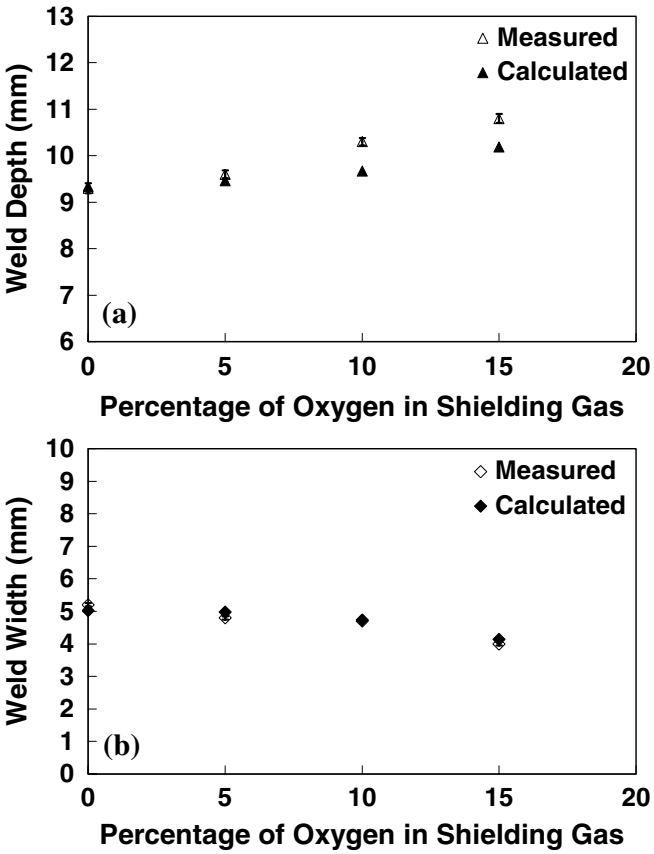

Figure 4. Comparison of the experimental and calculated laser welds (*a*) depths and (*b*) widths as a function of shielding gas O_2 percentage. Standard error bars are shown for measured weld dimensions.

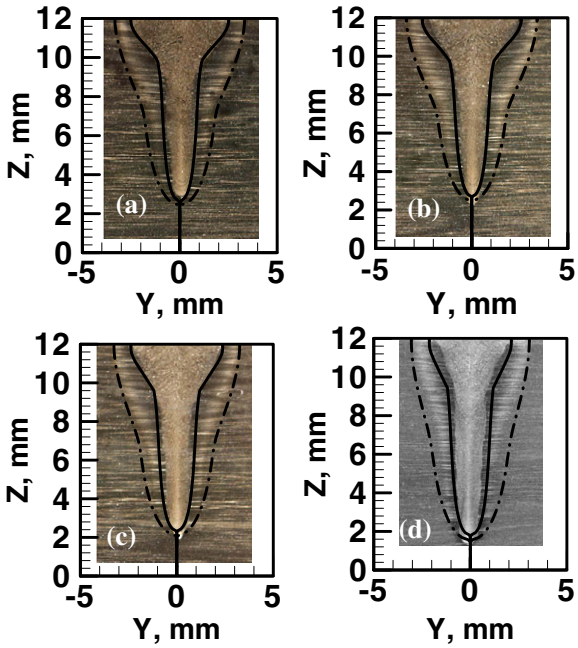

Figure 5. Comparison of experimental and calculated laser weld cross sections when welding with shielding gas containing (*a*) 0%, (*b*) 5%, (*c*) 10% and (*d*) 15% O_2. The dotted lines in the cross sections are the 1000 K isotherm and the solid line outlining the fusion zones is the 1745 K solidus isotherm.

inward flow is due to a more positive $d\gamma/dT$ with increasing concentrations of oxygen in the weld metal. As the inward fluid flow becomes more dominant, the weld pool width decreases. No significant vertical flow of liquid metal resulted from surface-tension gradients at the keyhole walls because the temperature gradients along the keyhole walls are small in keyhole-mode laser welding. For both 0 % and 10% O_2 cases, shown in figures 6(*a*) and (*b*), fluid velocities near the keyhole walls at short distances from the top surface are upwards whereas the flow direction is downwards farther away from the top surface. The similarities in flow patterns near the keyhole walls suggest that keyhole depth is not significantly affected by the fluid flow.

6. Conclusions

The effects of oxygen and sulfur in keyhole-mode high power Yb doped fibre laser welding of mild steel were evaluated both experimentally and theoretically. The experimental data on the effects of sulfur and oxygen on the weld pool depth and width were analysed statistically. The theoretical calculations were performed using a well tested numerical heat transfer and fluid flow calculations for keyhole-mode welding to seek phenomenological understanding.

The statistical data analysis showed that the measured weld penetration was not affected by the base-metal sulfur concentration but increased significantly with the O_2 content

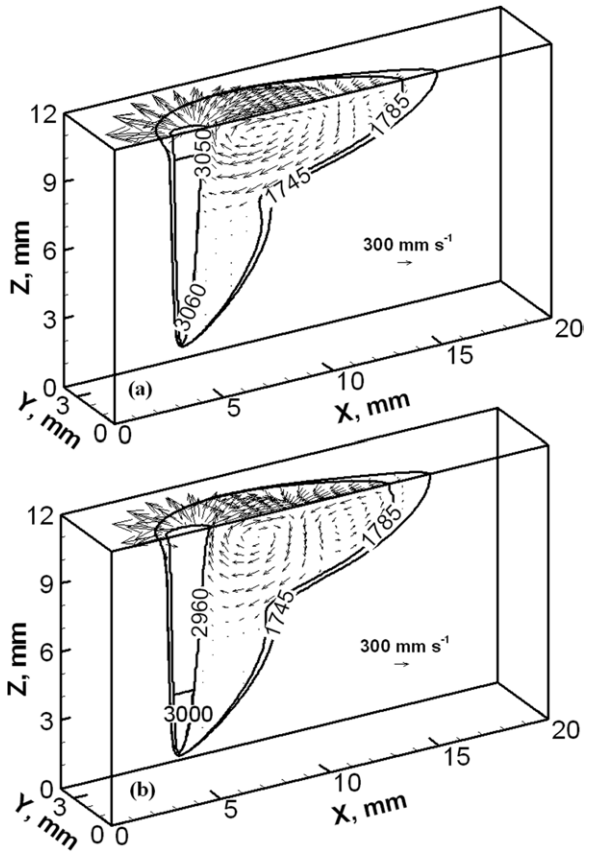

Figure 6. Temperature and fluid velocity profiles during 7 kW laser welding of mild steel when (*a*) 0% and (*b*) 10% O_2 is introduced to the shielding gas.

of the shielding gas. Measurements of the weld metal oxygen concentration revealed that increasing amounts of oxygen were dissolved in the weld pool as the O_2content of shielding gas was increased. The experimentally measured weld width decreased as the base-metal sulfur concentration or the oxygen content of shielding gas was increased. Computed results showed that the effects of sulfur and oxygen on weld width could be explained considering their influence on Marangoni convection. In weld pools containing either oxygen or sulfur, the flow of liquid metal on the weld pool surface very near the keyhole was always away from the keyhole while the direction of the flow was just the opposite close to the solid–liquid boundary. This behaviour is consistent with positive temperature coefficient of surface tension ($\mathrm{d}\gamma/\mathrm{d}T$) at temperatures close to the liquidus temperature of the steel and negative $\mathrm{d}\gamma/\mathrm{d}T$ at temperatures close to the boiling point of the alloy.

Convective flow of heat and mass in the weld pool was driven by the Marangoni flow at the weld pool surface and the resulting recirculation in the weld pool. At the keyhole walls, temperature gradients were small and, as a result, no significant vertical flow of the liquid metal resulted from surface-tension gradients at the keyhole wall. This behaviour is consistent with negligible changes in the depth of penetration of the weld with changes in sulfur concentration. Since computations showed no major differences in the liquid metal flow near the keyhole with changes in the oxygen concentration, Marangoni convection is not the source of increase in weld penetration with the concentration of oxygen. The increased weld penetration observed with the increased O_2 concentration of the shielding gas is consistent with the formation of CO at the keyhole wall from carbon and oxygen dissolved in the weld pool and increased pressure within the keyhole.

Acknowledgments

The authors would like to thank Dr G G Roy, Dr W Zhang and Dr L Zhao for helpful discussions.

Appendix: Calculation of F-test statistic

The sum of squares evaluates the variation of data within a group, between groups, and for the entire dataset. The sum of squares of variance between groups of observations is given by [48]

$$\mathrm{SS_B} = \sum_{j=1}^{J} n_j(\bar{y}_j - \bar{Y})^2, \tag{A1}$$

where J is the total number of groups of observations, n_j is the number of observations in the jth group, $\bar{y}_j$ is the mean of the particular jth group of observations and $\bar{Y}$ is the grand mean for all observations and groups. The grand mean is determined by [48]

$$\bar{Y} = \sum y_{ij}/N, \tag{A2}$$

where y_{ij} is the ith observed value for a particular group j and N is the total number of observations for all groups. The sum of squares which analyses the total variation for all observations is defined by [48]

$$\mathrm{SS_T} = \sum_{j=1}^{J}\sum_{i=1}^{n_j}(y_{ij} - \bar{Y})^2, \tag{A3}$$

where i is the number of observations in group j. The sum of squares for the variance within a group of observations is the difference of the sum of squares for the total variance of the dataset and the sum of squares for the variance between groups of observation and is given by [48]

$$\mathrm{SS_w} = \mathrm{SS_T} - \mathrm{SS_B}. \tag{A4}$$

The degrees of freedom normalize the calculations based upon their sample size and the number of groups considered and aid in providing a mean variance for the observations. The total degrees of freedom are given by [48]

$$\mathrm{d}f_\mathrm{T} = N - 1. \tag{A5}$$

The number of degrees of freedom between groups and within a group of observations are given by [48]

$$\mathrm{d}f_\mathrm{B} = J - 1, \tag{A6}$$

$$\mathrm{d}f_\mathrm{W} = N - J, \tag{A7}$$

where $\mathrm{d}f_\mathrm{B}$ is the degrees of freedom for between groups of observations and $\mathrm{d}f_\mathrm{W}$ is the degrees of freedom for within groups of observations.

The mean square is an adjusted measure of the variance within and between groups that considers the number of observations in the group and is used for calculating the ratio F. The mean square between and within groups of observations are given by [48]

$$\mathrm{MS_B} = \frac{\mathrm{SS_B}}{J-1}, \tag{A8}$$

$$\mathrm{MS_W} = \frac{\mathrm{SS_W}}{N-J}, \tag{A9}$$

where the subscripts B and W stand for between and within the groups of observations. The ratio of the mean squares gives the calculated F value for comparison with the critical F and is given by [48]

$$F = \frac{\mathrm{MS_B}}{\mathrm{MS_W}}. \tag{A10}$$

References

[1] Ribic B, Palmer T A and DebRoy T 2009 *Int. Mater. Rev.* **54** 223–44
[2] Zhao H and Debroy T 2003 *J. Appl. Phys.* **93** 10089–96
[3] Von Allmen M 1987 *Laser–Beam Interactions with Materials* (New York, NY: Springer)
[4] Aidun D K and Martin S A 1997 *J. Mater. Eng. Perform.* **6** 496–502
[5] Kutsuna M and Chen L 2002 Interaction of both plasmas in CO_2 laser–MAG hybrid welding of carbon steel *1st Int. Symp. on High-Power Laser Macroprocessing (Osaka, Japan, 27–31 May 2002)* (Osaka, Japan: SPIE—The International Society for Optical Engineering) pp 341–6
[6] Naito Y, Mizutani M and Katayama S 2006 *J. Laser Appl.* **18** 21–27
[7] Pitscheneder W, DebRoy T, Mundra K and Ebner R 1996 *Weld. J.* **75** S71–S80
[8] Zhao L, Tsukamoto S, Arakane G, Sugino T and Debroy T 2011 *Sci. Technol. Weld. Joining* **16**(2) 166–73
[9] Rao Z H, Zhou J, Liao S M and Tsai H L 2010 *J. Appl. Phys.* **107** 054905
[10] Hu J and Tsai H L 2008 *J. Phys. D: Appl. Phys.* **41** 065202
[11] Lowke J J, Tanaka M and Ushio M 2005 *J. Phys. D: Appl. Phys.* **38** 3438–45
[12] Mishra S, Lienert T J, Johnson M Q and DebRoy T 2008 *Acta Mater.* **56** 2133–46
[13] Tanaka M and Lowke J J 2007 *J. Phys. D: Appl. Phys.* **40** R1–R23
[14] Do-Quang M, Amberg G and Pettersson C O 2008 *Trans. ASME, J. Heat Transfer* **130** 092102
[15] Zhou J, Tsai H L and Lehnhoff T F 2006 *J. Phys. D: Appl. Phys.* **39** 5338–55
[16] Safdar S, Li L and Sheikh M A 2007 *J. Phys. D: Appl. Phys.* **40** 593–603
[17] Aalderink B J, de Lange D F, Aarts R G K M and Meijer J 2007 *J. Phys. D: Appl. Phys.* **40** 5388–93
[18] Limmaneevichitr C and Kou S 2000 *Weld. J.* **79** 231S–37S
[19] Wang Y and Tsai H L 2001 *Metall. Mater. Trans.* B **32** 501–15
[20] Zhao Y Z, Zhou H P and Shi Y W 2006 *Modeling Simul. Mater. Sci. Eng.* **14** 331–49
[21] Kou S and Sun D K 1985 *Metall. Trans.* A **16** 203–13
[22] DebRoy T and David S A 1995 *Rev. Mod. Phys.* **67** 85–112
[23] Rai R, Roy G G and DebRoy T 2007 *J. Appl. Phys.* **101** 054909
[24] Rai R, Elmer J W, Palmer T A and DebRoy T 2007 *J. Phys. D: Appl. Phys.* **40** 5753–66
[25] Ribic B, Rai R and DebRoy T 2008 *Sci. Technol. Weld. Joining* **13** 683–93
[26] Rai R, Kelly S M, Martukanitz R P and DebRoy T 2008 *Metall. Mater. Trans.* A **39A** 98–112
[27] Bird R B, Stewart W E and Lightfoot E N 1960 *Transport Phenomena* (New York: Wiley)
[28] He X, Elmer J W and DebRoy T 2005 *J. Appl. Phys.* **97** 084909
[29] Kumar A and DebRoy T 2003 *J. Appl. Phys.* **94** 1267–77
[30] Sahoo P, DebRoy T and McNallan M J 1988 *Metall. Trans.* B **19** 483–91
[31] Kaplan A F H, Mizutani M, Katayama S and Matsunawa A 2002 *J. Phys. D: Appl. Phys.* **35** 1218–28
[32] Lee J Y, Ko S H, Farson D F and Yoo C D 2002 *J. Phys. D: Appl. Phys.* **35** 1570–6
[33] Ki H, Mohanty P S and Mazumder J 2002 *Metall. Mater. Trans.* A **33** 1817–30
[34] Sudnik W, Radak D and Erofeew W 1998 *J. Phys. D: Appl. Phys.* **31** 3475–80
[35] Fuhrich T, Berger P and Hugel H 2001 *J. Laser Appl.* **13** 178–86
[36] Kaplan A 1994 *J. Phys. D: Appl. Phys.* **27** 1805–14
[37] Klein T, Vicanek M, Kroos J, Decker I and Simon G 1994 *J. Phys. D: Appl. Phys.* **27** 2023–30
[38] Kroos J, Gratzke U and Simon G 1993 *J. Phys. D: Appl. Phys.* **26** 474–80
[39] Lancaster J F 1986 *The Physics of Welding* (New York, NY: Pergamon)
[40] Poirier D R and Geiger G H 1994 *Transport Phenomena in Materials Processing* (Warrendale, PA: The Minerals, Metals, and Materials Society)
[41] Rai R, Burgardt P, Milewski J O, Lienert T J and DebRoy T 2009 *J. Phys. D: Appl. Phys.* **42** 025503
[42] Fruehan R J, United States Steel Co., American Society for Metals 1999 *The Making, Shaping and Treating of Steel* vol Steelmaking and Refining Volume (Pittsburgh, PA: AISE Steel Foundation)
[43] Rosenqvist T 2004 *Principles of Extractive Metallurgy* (Trondheim, Norway: Tapir Academic Press)
[44] Sigworth G K and Elliott J F 1974 *Met. Sci.* **8** 298–310
[45] Limmaneevichitr C and Kou S 2000 *Weld. J.* **79** 126S–35S
[46] Brandes E A and Brook G B 1992 *Smithells Metals Reference Book* (Woburn, MA: Butterworth-Heinemann)
[47] Tsukamoto S, Zhao L, Arakane G, Sugino T and Yasuda K 2009 Prevention of porosity in deep partial penetration laser and hybrid welding with minimum solute oxygen in the weld metal *Int. Congress on Applications of Laser and Electro-Optics* (Orlando, FL: Laser Institute of America)
[48] Dalgaard P 2002 *Introductory Statistics with R* (New York: Springer)
[49] Rai R, Palmer T A, Elmer J W and Debroy T 2009 *Weld. J.* **88** 54S–61S